



HAL
open science

Unprecedented Molecular Diversity Revealed in Meteoritic Insoluble Organic Matter: The Paris Meteorite's Case

Grégoire Danger, Alexander Ruf, Julien Maillard, Jasmine Hertzog, Vassilissa Vinogradoff, Philippe Schmitt-Kopplin, Carlos Afonso, Nathalie Carrasco, Isabelle Schmitz-Afonso, Louis Le Sergeant D'hendecourt, et al.

► To cite this version:

Grégoire Danger, Alexander Ruf, Julien Maillard, Jasmine Hertzog, Vassilissa Vinogradoff, et al.. Unprecedented Molecular Diversity Revealed in Meteoritic Insoluble Organic Matter: The Paris Meteorite's Case. *The Planetary Science Journal*, 2020, 1 (3), pp.55. 10.3847/psj/abb60f. insu-02982054v1

HAL Id: insu-02982054

<https://hal.science/insu-02982054v1>

Submitted on 22 Apr 2021 (v1), last revised 28 Oct 2020 (v2)

HAL is a multi-disciplinary open access archive for the deposit and dissemination of scientific research documents, whether they are published or not. The documents may come from teaching and research institutions in France or abroad, or from public or private research centers.

L'archive ouverte pluridisciplinaire **HAL**, est destinée au dépôt et à la diffusion de documents scientifiques de niveau recherche, publiés ou non, émanant des établissements d'enseignement et de recherche français ou étrangers, des laboratoires publics ou privés.

1
2
3
4
5
6
7
8
9
10
11
12
13
14
15
16
17
18
19
20
21
22
23
24
25
26
27
28
29
30
31
32
33
34
35
36
37
38
39
40
41

Main Manuscript for

Unprecedented molecular diversity revealed in meteoritic insoluble organic matter: The Paris meteorite's case

Grégoire. Danger^{1,2,3*}, Alexander Ruf¹, Julien Maillard^{4,5}, Jasmine Hertzog^{6,7}, Vassilissa Vinogradoff^{1,2}, Philippe Schmitt-Kopplin^{6,7}, Carlos Afonso⁴, Nathalie Carrasco⁵, Isabelle Schmitz-Afonso⁴, Louis Le Sergeant d'Hendecourt^{1,2}, Laurent Remusat⁸.

¹ Laboratoire de Physique des Interactions Ioniques et Moléculaires, UMR 7345, Aix-Marseille Université, CNRS, Centre de St-Jérôme, Marseille, France

² Aix Marseille Université, CNRS, CNES, LAM, Marseille, France

³ Institut Universitaire de France (IUF)

⁴ Normandie Univ, COBRA UMR 6014 et FR 3038 Univ Rouen; INSA Rouen; CNRS IRCOF, 1 Rue Tesnière, 76821 Mont-Saint-Aignan Cedex France

⁵ LATMOS/IPSL, Université Versailles St Quentin, UPMC Université Paris 06, CNRS, 11 blvd d'Alembert, F-78280 Guyancourt, France

⁶ Helmholtz Zentrum München, Analytical BioGeoChemistry, Neuherberg, Germany

⁷ Technische Universität München, Chair of Analytical Food Chemistry, Freising-Weihenstephan, Germany

⁸ Muséum National d'Histoire Naturelle, Sorbonne Université, UMR CNRS 7590, Institut de minéralogie, de physique des matériaux et de cosmochimie, Paris, France

Corresponding author: Grégoire Danger

Email: gregoire.danger@univ-amu.fr

Keywords: Insoluble Organic Matter (IOM) – meteorites – LDI-FT-ICR-MS(/MS)

Author Contributions : G.D. designed research; L.R. and V.V. performed Paris IOM isolation; G.D. and J.M. performed LDI-FT-ICR-MS(MS) analyses; G.D., A.R., J.M., and J.H. performed data treatments; G.D. wrote the paper and A.R., J.M, J.H., V.V., P.S-K, C.A, L.R., N.C., I.S-A, L.S.H contributed to the paper writing.

Abstract

The insoluble organic matter (IOM) contained in carbonaceous chondrites has witnessed a diverse suite of processes possibly starting from the evolution of the parent molecular cloud down to the protosolar nebula and finally to asteroidal processes that occurred on the chondrites parent bodies. Laser desorption coupled to ultra-high-resolution mass spectrometry reveals that the IOM of the Paris meteorite releases a large diversity of molecules. Various molecular families ranging from hydrogenated amorphous carbon to CHNOS aromatic molecules were detected with heteroatoms (nitrogen, oxygen, and sulfur) mainly incorporated within aromatic structures. Molecules bearing nitrogen atoms present a significant variation in aromaticity. These unprecedented results allow proposing that small molecules bearing heteroatoms could be trapped in the large macromolecular network of the IOM by hydrophobic interactions. This molecular diversity could originate from different sources, such as the SOM, the hydrothermal alteration inside the Paris's parent body, or even generated during the IOM extraction procedure. **It has to be noted that some of the molecular diversity may reflect fragmentation and rearrangement of the IOM constituents during the laser desorption ionization, although care was taken to minimize such damage.**

42 1. Introduction

43 Carbonaceous chondrites (CCs) are fragments of primitive asteroids that are known to contain up to 6 wt.% of
44 organic matter (OM) (Pearson et al. 2006). The insoluble organic matter (IOM) represents the major organic
45 carbon component of CCs (75 to 95 wt.% of the total recovered organic matter) (Pizzarello, S.; Cooper, G. W.;
46 Flynn 2006; Remusat 2015; Ruf et al. 2018; Schmitt-Kopplin et al. 2010; Sephton 2002). Its isotope
47 compositions, in particular the D/H ratio, indicate that it derives from precursors possibly originating from the
48 interstellar medium or the cold regions of the outer solar system that were subsequently accreted on the CC
49 parent bodies (Remusat et al. 2010). Analyses reveal that the IOM is constituted of aromatic units, up to
50 coronene (seven-ring units), with 20-30 % of aliphatic structures, mainly in the form of bridges between these
51 structures (Cody et al. 2002; Cody & Alexander 2005; Gardinier et al. 2000; Orthous-Daunay et al. 2013;
52 Remusat et al. 2005a; Yabuta et al. 2005), up to seven carbon atoms for the aliphatic bridges and four carbons
53 for the side chains on the aromatic units (Remusat et al. 2005a). Heteroatoms also compose the IOM with up to
54 20 % of oxygen and only 3 % of nitrogen, roughly reflecting cosmic abundance ratios of these two elements.
55 Oxygen is mainly in the form of ether and ester groups (Hayatsu et al. 1977; Remusat et al. 2005b, 2005a) but
56 also in the form of furans, contributing to the aromatic units (Cody et al. 2011). Nitrogen can occur in nitrile
57 groups or inside heterocycles such as pyrroles (5-membered rings) (Remusat et al. 2005a). The amount of sulfur
58 is equivalent to nitrogen and is involved in thiophene structures, as well as sulfoxide and sulfone in the aliphatic
59 chains (Orthous-Daunay et al. 2010; Remusat et al. 2005a). As a result, the IOM is schematically represented as
60 a cross-linked structure of aromatic and aliphatic units with some heteroatoms, constituting macromolecules
61 (Derenne & Robert 2010). This complex macromolecular assemblage would have an approximate global
62 composition of $C_{100}H_{60-80}O_{16-18}N_3S_{2-7}$ (Alexander et al. 2007; Derenne & Robert 2010). Its condensed structure
63 made the IOM resistant to secondary processes that occurred during the parent body evolution. Therefore, **the**
64 **IOM includes rare components that record** the conditions that occurred during the evolution of the molecular
65 cloud into the solar system (Remusat 2015).

66 We choose the Paris meteorite because **it experienced a minimal thermal alteration, and is** the least **aqueous**
67 **altered of any CM chondrite reported to date.** Found in 2012, the Paris meteorite has been classified as an
68 unmetamorphosed chondrite, 2.7-2.9 CM in the aqueous alteration scale defined by Rubin et al. (Rubin et al.
69 2007). Its peculiar mineralogical heterogeneities, the significant porosity, the persistence of Fe-Ni metal (usually
70 absent in CMs), the presence of amorphous silicates and nanosulfides in the matrix imply that the Paris CM
71 chondrite only experienced a quite mild/gentle hydrothermal period **compared to other CM meteorites**
72 (Hewins et al. 2014; Leroux et al. 2015; Marrocchi et al. 2014). Previous analysis of Paris IOM revealed a lower
73 aromatic/aliphatic carbon ratio than other CMs, and a lower content of oxygen atoms (Vinogradoff et al. 2017),
74 but globally the same macromolecular assemblages as described above.

75 In this contribution, we report new results obtained from laser desorption ionization (LDI) coupled to an ultra-
76 high-resolution mass spectrometer (FT-ICR-MS) on a Paris IOM. The LDI is well-suited for the analysis of IOM
77 due to the low volatility and solubility of the involved components. With this technique direct information are
78 obtained on the molecular content of this Paris IOM sample by preventing as much as possible the molecule
79 degradation before their detection. The coupling of LDI with a high-resolution mass spectrometry then allows
80 obtaining information on the molecular diversity present in this IOM. We indeed reveal new and original
81 information on the molecular composition, diversity and aromaticity of the Paris IOM that can be related to
82 synthesis environments during the early ages of the solar system.

83 2. Methods

84 2.1 Isolation of the Paris IOM.

85 The isolation of the Paris IOM is described by Vinogradoff et al. (Vinogradoff et al. 2017) and reported
86 hereafter. About 15 g of the Paris meteorite were provided by the Muséum National d'Histoire Naturelle, Paris,
87 France. Matrix and chondrules were separated (Göpel et al. 2015). A matrix-enriched sample was crushed in an
88 agate mortar and IOM was subsequently isolated using the protocols described in (Remusat et al. 2005b;
89 REMUSAT et al. 2008). In brief, the powdered matrix was subjected to several extractions in water, acetone and

90 dichloromethane/methanol (2:1, vol/vol). The solid residue was then subjected to HF/HCl treatment by stirring
91 in a mixture of HF/HCl (16N/6N, 2:1, vol/vol) for 24 h at room temperature under nitrogen flux. The residue
92 was then washed many times with HCl (6N) for 2 h at 70 °C (i.e., to remove fluoride precipitates) until the final
93 solute was colorless. The acid residue was then washed 10 times with water, extracted 3 times with acetone and a
94 mixture of CH₂Cl₂/MeOH, 2:1 vol/vol and dried under nitrogen. A residue of about 150 mg was recovered.

95 2.2 Paris IOM analysis by LDI FT-ICR-MS(MS)

96 All analyses were performed in Rouen, France on a FT-ICR Solarix XR mass spectrometer (Bruker Daltonics
97 Germany) equipped with a 12 Tesla superconducting magnet and a laser desorption ionization source (laser
98 NdYAg×3 355 nm). The mass spectrometer was externally calibrated with a solution of sodium trifluoroacetate.
99 One mg of the Paris IOM was crushed and about 0.1 mg were deposited on a LDI plate without any additional
100 matrix (Barrère et al. 2012). Mass spectra were obtained using the broadband mode from m/z 110.6 to m/z
101 1,200.0 with the sum of 400 scans in positive ion mode. The analogical signal was amplified and digitalized with
102 16 million points resulting in the recording of transient of 5 s which was transformed into the corresponding
103 frequency domain by Fourier transform (one zero fill and full sine apodization). This resulted in magnitude mode
104 spectra with a mass resolving power (resolution) of 1.100.000 at m/z 400. No signals relative to the Paris IOM
105 signature were detected in blanks (Appendix A1). All spectra were phased, and the resulting absorption mode
106 spectrum had a resolution of 2.500.000 at m/z 400 (Qi et al. 2012). The following instrumental parameters were
107 implemented: Plate offset 100 V, Deflector plate 210 V, Laser power 11% (0.25 µJ) or 13% (0.30 µJ), spot size
108 30 µm, fluence at 11% 36.7 mJ/cm² and at 13% 42.26 mJ/cm², laser shots 50, laser shots frequency 1000 Hz,
109 funnel 1 at 150 V, skimmer 1 at 25 V. Compared to LDI-TOFMS, FT-ICR presents a higher sensitivity and
110 resolution.

111 For tandem mass spectrometry experiments (MS/MS), several nominal masses were isolated in a quadrupole and
112 then fragmented by acceleration in a collision cell filled with argon. This Collision Induced Dissociation (CID)
113 allows achieving a controlled fragmentation by adjusting the value of the imposed acceleration voltage (the
114 higher the voltage, the greater is the fragmentation). The same parameters were used for the MS and MS/MS
115 experiments, except for the laser power that was raised to 25% of the nominal laser power (thus, 0.58 µJ) and the
116 number of shots was increased to 200 in order to obtain a decent signal.

117 LDI ionization techniques is well suited to analyze insoluble organic materials. However, a drawback of these
118 techniques is the possibility to fragment and recombine the organic compounds if the laser energy is not well
119 tuned (Aubriet et al. 2018; Wu et al. 2013). In order to avoid these phenomena, different laser powers were
120 tested (11%, 13%, and 20%). From the achieved mass spectra profiles (See Appendix 2), it is assumed that the
121 11% laser power impedes the formation of artefacts and mainly molecular ions are detected in the form of
122 [M+H]⁺ and [M]²⁺. Furthermore, a laser power lower than 11% gave same spectral signatures but with an
123 important sensitivity decrease implying that 11% provides the best compromise between sensitivity and
124 limitation of fragmentations. In optimized conditions, LDI ensures detecting compounds over a similar mass
125 range but with different chemical properties (more aromatic) from ESI (Maillard et al. 2018). Higher-masses
126 molecules were observed with a laser power of 13% and 20% as compared to those obtained at 11%. **For**
127 **instance, at 11% the energy is not sufficient to ionize native fullerene or to generate them by molecular**
128 **recombinations since fullerenes are not observed, certifying the detection of a large fraction of native**
129 **molecules and not generated at 11%.**

130 2.3 Data treatment

131 Compass DataAnalysis 5.0 software (Bruker Daltonics, Germany) was used to process the FT-ICR mass
132 spectrum. The mass spectrum was first calibrated with a list of well-characterized ions from hydrocarbon and
133 fullerene (C₄₈₋₇₄) molecular series. The mass accuracy achieved for these ions was comprised between ± 200
134 ppb. A peak list at signal-to-noise ratio (S/N) greater than 6 was generated and magnetron and satellite signals
135 were removed as previously reported (Kanawati et al. 2017). The filtered mass list was then subject to
136 assignment by means of Composer software (Sierra Analytics, Modesto, CA). Thus, both protonated and radical
137 cations were assigned with general formulas C₀₋₂₀₀H₀₋₁₀₀₀O₀₋₆N₀₋₆S₀₋₆ within a 0.4 ppm mass accuracy window

138 and DBE ranging from -0.5 to 100. Error plots for assignment validation are shown in Appendix A3. Thousands
139 of features were achieved that belong to different heteroatom classes. Further data processing was performed via
140 Python.

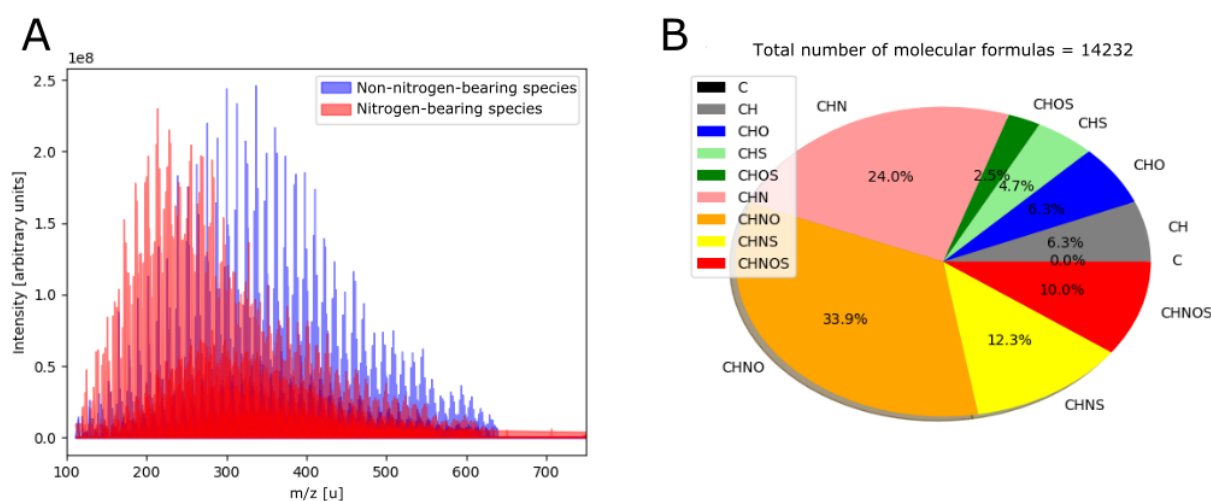
141 *Calculation of X_C .* The aromaticity equivalent X_C was calculated, according to the following formula (Yassine et
142 al. 2014): $X_C = ((2 \times n(C) + n(N) - n(H) - 2 \times m \times n(O)) / (DBE - m \times n(O))) + 1$ with $DBE = n(C) - n(H)/2 + n(N)/2$
143 $+ 1$, where m corresponds to an estimate of the oxygen fraction linked to carbon by double bonds; $m = 0.75$
144 based on NMR data (Vinogradoff et al. 2017). Chemical classes, aliphatics, aromatics and condensed aromatics
145 were defined accordingly: aliphatics $0 < X_C < 2.5$; aromatics (one aromatic ring, like benzene) $2.5 < X_C < 2.7$ and
146 condensed aromatics (more aromatic rings like in PAH) $2.7 < X_C$. From these X_C values, the degree of
147 aromaticity will be estimated based on the distribution between condensed aromatics, aromatics and aliphatics.

148 3. Results

149 3.1 Molecular diversity in Paris IOM

150 The LDI-FT-ICR mass spectrum of the Paris IOM presents a large number of signals from which 14232
151 molecular formulas were assigned (Figure 1). To obtain information on the carbon skeleton of molecules, the
152 degree of aromaticity was estimated for each molecular formula (estimated from the aromaticity factor X_C ,
153 details in Appendix A4). Condensed aromatic structures correspond to 90.9% of these attributions. Aromatic
154 structures represent 6.9% and only 2.2% of these attributions are referred to aliphatic ones. This aromaticity
155 description is relevant to the general view of IOM structures, which is mainly considered as highly aromatic with
156 few aliphatic bridges cross-linking the aromatic structures.

157 Among the 14232 attributed ions, eight different chemical families could be differentiated (Figure 1B).
158 Nitrogen-bearing species represent 80.2% of the molecular attributions with the CHNO family representing
159 33.9% of the total formulas (Figure 1B). It is known that LDI privileges ionization of PAH's bearing basic
160 functions such as nitrogen chemical groups. This difference in the number of attributed ions can thus be
161 amplified by the ionization technique that we used (Cho et al. 2013). For non-nitrogen-bearing species, CH and
162 CHO families are the most abundant ones, with 6.3% of the total attributions for each. In Figure 1A, the mass
163 spectrum also presents separately the mass distributions related to nitrogen-bearing attributions (in red) and non-
164 nitrogen-bearing species (in blue). While the non-nitrogen-bearing families do present a homogenous maximum
165 in peak intensity at 330 u, two different mass distributions are clearly distinguishable among the nitrogen-
166 bearing species (see also Appendix A5). When the number of heteroatoms increases (O, S or O+S), the
167 maximum varies from 230 u for CHN to 330 u for CHNOS.



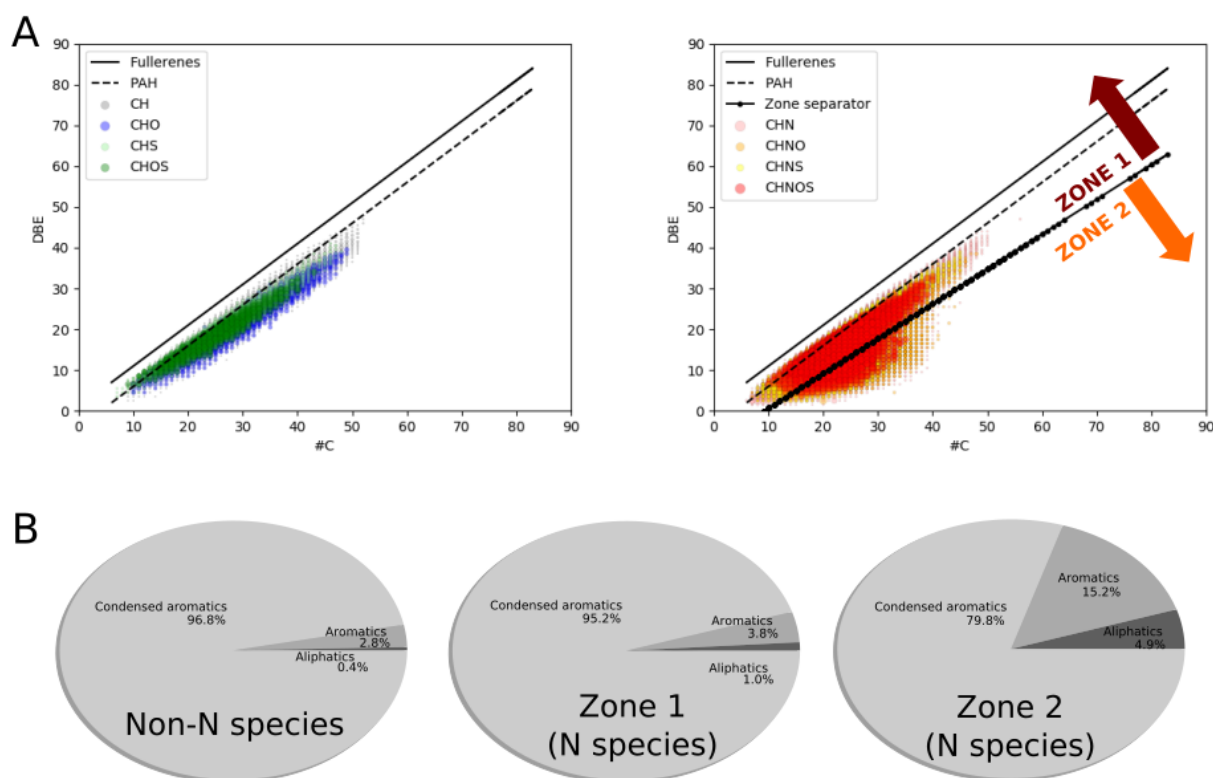
168

169 **Figure 1** – Distributions of nitrogen and non-nitrogen-bearing species in the LDI-FT-ICR mass spectrum (laser
170 energy of 11%) of Paris IOM (A) and (B), partition of the 14232 attributions in chemical families (C, CH, CHO,
171 CHS, CHOS, CHN, CHNO, CHNS or CHNOS).

172 These chemical families can be displayed using DBE (double bond equivalent) vs number of carbons (#C) plots,
 173 highlighting the different distributions (Figure 2A). The non-nitrogen-bearing families present a homogenous
 174 trend near the PAH lines implying that these molecules are mainly polycondensed aromatic structures. The
 175 evaluation of the degree of aromaticity (via Xc) presents condensed structures at 97% for the non-nitrogen-
 176 bearing attributions (Figure 2B), with a number of hydrogen atoms more than half times lower than the number
 177 of carbon (Appendix A5).

178 Compared to the non-nitrogen-bearing species, nitrogen-bearing ones present two different distributions, divided
 179 into Zones 1 and 2 (Figure 2B and 11A) relatively to the non-N bearing species. One observes a similar trend as
 180 the non-nitrogen-bearing families (zone 1), while the second represents lower DBE values suggesting a lower
 181 degree of aromaticity (Appendix A5). This is confirmed by the degree of aromaticity where zone 1 is similar to
 182 the non-nitrogen-bearing species, while zone 2 presents lower amounts of condensed aromatics and higher
 183 amounts of aromatic and aliphatic structures (Figure 2B). By separating the nitrogen-bearing families in these
 184 two zones, we observe that zone 1 follows the PAH line of the non-nitrogen-bearing families, with a similar H/C
 185 atomic ratio (~0.6). Zone 2 however, presents lower DBE/#C ratios, and a much higher H/C (1.2), implying
 186 species containing the lowest number of condensed aromatic structures (79.8 %) and the highest number of
 187 aliphatic structures (4.9 %). Zone 1 and zone 2 hence present different molecular carbon skeletons. Nonetheless,
 188 each zone contains the same number of O and N relative to carbon, with only weaker amounts of S relative to C
 189 for zone 2 (Appendix A5).

190

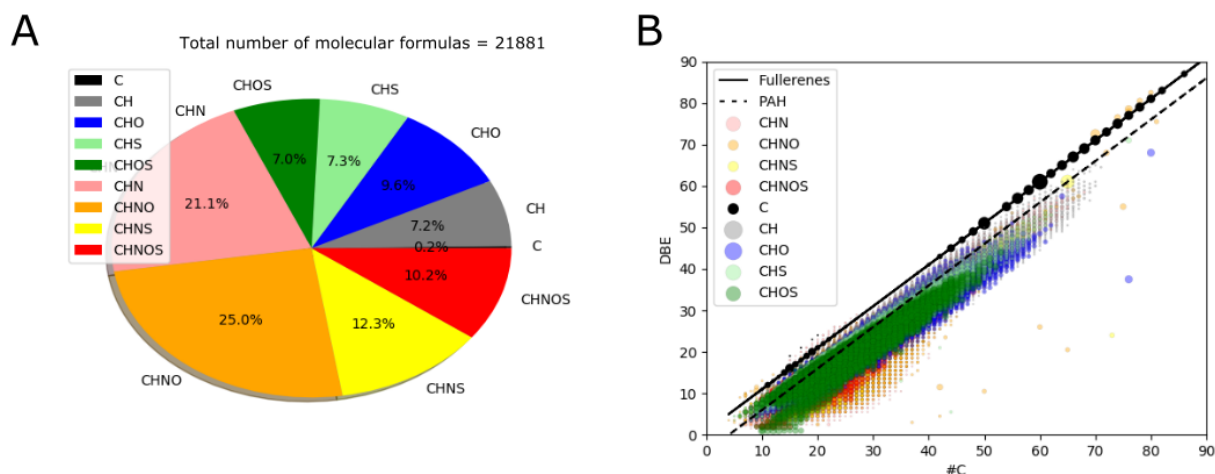


191
 192 **Figure 2** – Double Bond Equivalent (DBE) versus the number of carbon (#C) for each molecular formula is
 193 plotted, with the dotted line indicating the PAH trend, the full line indicating fullerenes composition and a
 194 separator line between both distributions observed for nitrogen-bearing species (A). Xc pie chart of the three
 195 distinct distributions, showing the proportions of condensed aromatic, aromatic and aliphatic structures (B).
 196 Laser energy at 11% of the laser power.

197 **3.2 Higher mass molecular content and pure carbon structures**

2198 We tested for the presence of PAH like structures in the Paris IOM by varying the laser power between 11, 13
 2199 and 20% (Santos et al. 2016; Wang et al. 2020). The laser power corresponds to the amount of energy that
 2200 impacts the sample to obtain desorption and ionization of molecules. It has to be noted that depending of the
 2201 laser energy, secondary reactions could occur such as pyrolysis and molecular recombination. Consequently, it is
 2202 important to carefully evaluate the impact of the laser power percentage as described in Appendix A2 that
 2203 estimate at 11% the energy limiting these recombinations. With the 13% laser power analysis, the number of
 2204 attributions increases from 14232 to 21881 (Figure 3A), potentially reflecting the thermal heating effect
 2205 generated by the laser spot, which then allows for the desorption of new species with lower net vapor pressure.
 2206 Furthermore, the family distribution is directly impacted (Figure 3A). Nitrogen-bearing families are still the most
 2207 abundant but their relative percentage drops to 68.6%. This is clearly due to an increase in the number of non-
 2208 nitrogen-bearing attributions. Especially, CHOS and CHS do increase to 7.0% (vs. 2.5%) and 7.3% (vs. 4.7%),
 2209 respectively of the total attributions. Furthermore, some pure carbon structures do appear and represent 0.2%.
 2210 This increase in the number of non-nitrogen-bearing species at higher laser power could imply that these species
 2211 represent large condensed structures presenting higher desorption energies (Appendix A6).

2212 DBE vs #C for attributions at the 13% laser power analysis (Figure 3B) shows that for higher laser power the
 2213 number of attributions presenting a higher DBE increases for a same carbon number. Indeed, a higher number of
 2214 attributions is observed between PAHs and pure carbon lines, confirming an increase of the degree of
 2215 aromaticity of the detected ions ($H/C=0.81$ for 11% vs. $H/C=0.60$ for 13%). The combination of analyses at 11%
 2216 and 13% laser power shows a significant molecular diversity in the Paris IOM in terms of number of released
 2217 molecules but also in their degree of aromaticity. Indeed, higher masses of species containing up to 90 carbons
 2218 are also detected, with the presence of fullerene-like structures and particularly the C_{60} molecule at 719.99952 u.
 2219 This detection would corroborate the previous detection of C_{60} in meteorites (Becker et al. 1996, 2000).
 2220 However, we cannot confidently state if fullerene species are natively present in the IOM or if they are generated
 2221 by the ionization process (Pereira et al. 2014; Santos et al. 2016) during the measurements in our LDI FT-ICR-
 2222 MS. The higher sensitivity in the fullerene detection at 20% laser power tends to promote degradation and
 2223 fragmentation of the native molecules, resulting in a higher detection of fullerenes (Appendix A2). Nevertheless,
 2224 this process demonstrates that IOM contains also the carbon structures that could be related to rather large PAH
 2225 molecules, even if molecular ions detected at higher laser power could come from recombination (Aubriet et al.
 2226 2018; Wu et al. 2013).



2227
 2228 **Figure 3 – Distribution** of the chemical families observed in our Paris IOM with power laser energy of 13%
 2229 (A). Double Bound Equivalence (DBE) as a function of the number of carbon (#C) for the same families (B).
 2230 Slopes of pure PAHs and pure carbon (fullerenes) structures are also reported for references.

2231 3.3 Insights into molecular structures

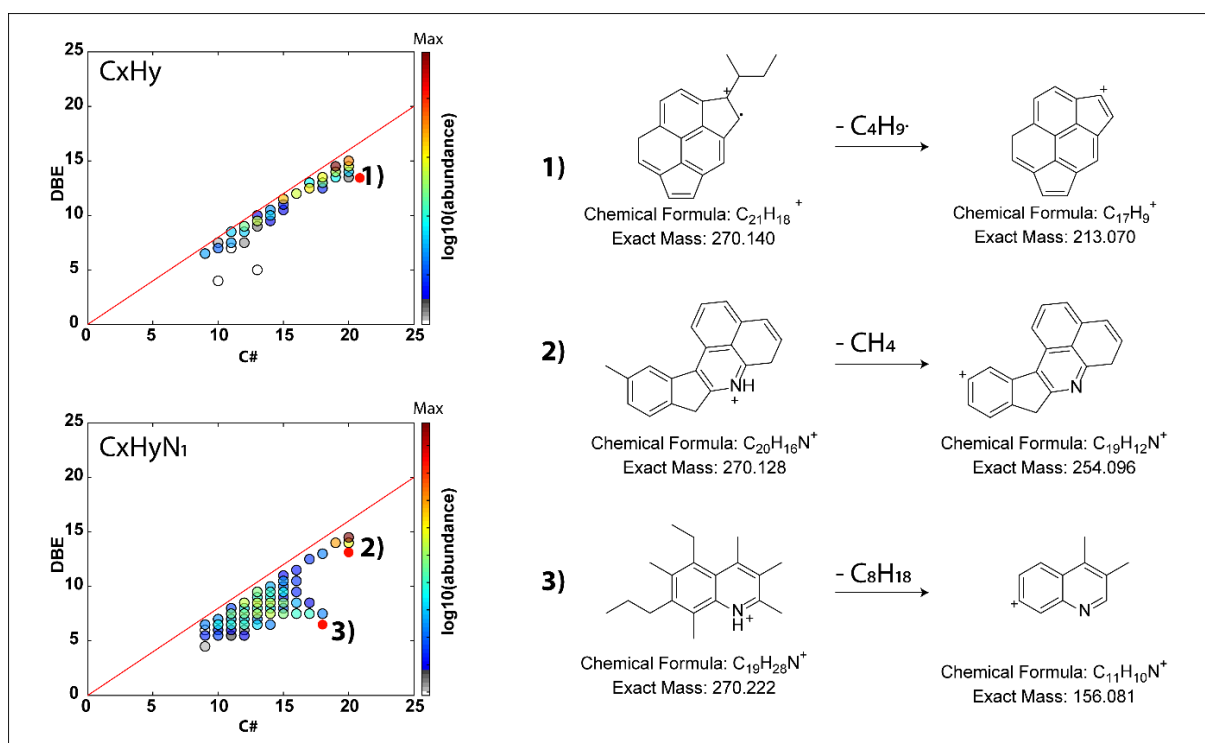
2232 To obtain information about the structures of molecules released from the IOM, collision induced dissociation
 2233 (CID) experiments were performed on some selected precursor ions. For condensed aromatic structures, two
 2234 structural models exist concerning the cores of such compounds: i) aromatic cores linked by aliphatic bridges

235 (archipelago type), and ii) a single large aromatic core with several aliphatic carbon ramifications (island type).
236 Each model has a typical fragmentation pattern in CID experiments (Chacón-Patiño et al. 2017, 2018a, 2018b;
237 Le Maître et al. 2019). In the present case, we will focus on hydrocarbon molecules (C_xH_y) and mono nitrogen
238 compounds ($C_xH_yN_1$) at the m/z 270 nominal mass (a second example at m/z 306 is also reported in the
239 Supporting Information showing the same type of characteristic fragmentation, Figure 14).

240 The C_xH_y molecular ions (Figure 4, 1) are radical cations. Regarding the DBE vs #C plots, many fragments are
241 observed following the PAH line (red line). In Figure 4, from the m/z 270.140 ($C_{21}H_{18}^{+\bullet}$) precursor ion, the most
242 intense detected fragment ions series is produced through losses of alkyl radicals ($C_nH_{2n+2}^\bullet$) (Figure 15, 20 eV).
243 The corresponding bar plot, displaying this ion series, shows a major fragment at #C = 17 when the collision
244 energy is increased (Figure 15, 30 eV, 40 eV and 50 eV). Thus, this fragment ion should be a fully de-alkylated
245 aromatic core. As the precursor ion is a cationic radical, the main fragmentation scheme involves losses of alkyl
246 radical groups. As there is mainly no loss of DBE during fragmentation this compound should be an island type
247 structure (Chacón-Patiño et al. 2018b). Among the many possible isomers, a hypothetical formula of the
248 molecule and its corresponding fragmentation pattern is given in Figure 4, 1) and Figure 16A. The large number
249 of fragments indicates a high number of isomers for each precursor ion (Ruf et al. 2019).

250 The second (Figure 4, 2) and third examples (Figure 4, 3) focus on species containing one nitrogen atom
251 ($C_xH_yN_1$) in their molecular formula. Because these represent protonated molecules $[M+H]^+$, we assume that
252 they present a basic pyridine-type core (Figure 16B and 16C). Pyridine-type cores are privileged over pyrrole-
253 type cores because they are detected in positive mode, while pyrroles are detected in negative mode. Considering
254 island type molecules, losses of small alkanes (C_nH_{2n+2}), with the fragment ions keeping the nitrogen atoms are
255 mainly observed (Le Maître et al. 2019). It is therefore possible to recover the specific ions from this precursor
256 by extracting ion series containing one nitrogen atom. Two isobaric $C_xH_yN_1$ species were fragmented, one in
257 zone 1 and the other in zone 2 of the DBE/#C (Figure 2A). From the protonated precursors, mainly losses of
258 alkane molecules are detected. Both molecules are fitted with the island model regarding the DBE plots and
259 barplots. However, the ones in zone 2 have a different fragmentation pattern (Figure 16C) as the de-alkylation
260 process is more pronounced. It means that this molecule presents a higher alkylation than in zone 1. This effect is
261 only observed for N-bearing molecules.

262 These CID experiments demonstrate that hydrocarbon species (C_xH_y) and nitrogenated ones ($C_xH_yN_1$, zone 1)
263 follow mainly a low alkylated island structural pattern whereas some other nitrogenated species have a highly
264 alkylated island pattern ($C_xH_yN_1$, zone 2) (Figure 14). The nitrogen containing molecules bear either highly
265 aromatic compartments with a low degree of branching (zone 1) or compartments presenting a high number of
266 ramifications (zone 2). Fragmentation patterns of $C_xH_yO_1$ and $C_xH_yS_1$ families are also reported in supporting
267 information. These two other families seem to correspond to low-alkylated island type molecules (PAH like
268 structures), bearing their heteroatoms (O and S) in the aromatic cores of their structures (Figure 17).



269

270 **Figure 4** - Collision induced dissociation (CID) fragmentation experiments for IOM Paris, laser energy of 25%.
 271 DBE vs C# plots of the CH family CID energies at 40 eV of *m/z* 270, or DBE vs #C maps of the CHN₁ families
 272 with CID fragmentation at 40 eV of *m/z* 270. Example of formulas of the molecule and its corresponding
 273 fragmentation pattern are also reported.

274 4. Discussion

275 Based on comprehensive analyses, chondritic IOM is generally considered as cross-linked macromolecular
 276 structures, including heteroatoms, distributed either in aromatic units or in the aliphatic chains (Derenne &
 277 Robert 2010). This investigation on the Paris meteorite, shows that a fraction of molecules with low masses is
 278 part of this IOM. Indeed, even if we cannot exclude that some molecular ion detected could share covalent bonds
 279 with the macromolecular structure (see method section), the used low laser energy shows that a part of the Paris
 280 IOM is made of small units with masses ranging from 100 to 700 u. In addition, a significant molecular diversity
 281 is also present with various molecular series ranging from CH to CHNOS molecules. These molecules are
 282 mainly condensed aromatic structures with aliphatic substituents. Furthermore, heteroatoms are rather included
 283 in aromatic rings than in aliphatic chains owing to the observed fragmentation patterns. Elemental atomic ratios
 284 of this distribution (Table 1) give values (H/C=0.81, N/C=0.07, O/C=0.07 and S/C=0.04) near the ones observed
 285 from previous bulk elemental analysis of Paris IOM (H/C=0.71, N/C=0.04, S/C=0.09) (Vinogradoff et al. 2017).
 286 We observe that this fraction of Paris IOM presents a lower O/C ratio and a higher aliphatic/aromatic ratio than
 287 other IOMs from CMs (Alexander et al. 2007). The higher N/C can also be due to the pristine nature of the Paris
 288 IOM but we cannot exclude artefacts due to LDI ionization that tends to favor ionization of PAH's bearing
 289 nitrogen functions (Cho et al. 2013). Compared to the SOM analysis of meteorites, the molecules observed by
 290 LDI-FT-ICR-MS present an interesting similar molecular diversity (Hertkorn et al. 2015; Schmitt-Kopplin et al.
 291 2012, 2010) However, their aromaticity is much more pronounced (H/C=1.55 for Murchison SOM).
 292 Furthermore, O/C is lower than the one observed in Murchison (O/C=0.2) for instance, while a rather similar
 293 N/C is observed (Murchison, N/C=0.03). These molecules clearly present numerous characteristics with other
 294 IOM analyses in term of aromaticity and heteroatom content, but with a molecular diversity reminding the SOM
 295 one.

296

297 **Table 1.** For each detected family, are reported their number of attributions and their average molecular formula.
 298 Are also reported the ones for zone 1 and 2 of nitrogen species, the whole nitrogen species, the non-nitrogen
 299 species as well as for the total attributions. Data for 11% and 13% of the laser power are displayed.

Average molecular formula		Number of formula attributions		Chemical Families
11%	13%	11%	13%	
$[C_{58}]^+$	$[C_{40}]^+$	1	45	C
$[C_{33}H_{17}]^+$	$[C_{38}H_{16}]^+$	895	1577	CH
$[C_{29}H_{18}O_2]^+$	$[C_{32}H_{17}O_2]^+$	890	2091	CHO
$[C_{27}H_{14}S]^+$	$[C_{30}H_{14}S_2]^+$	666	1601	CHS
$[C_{25}H_{15}OS]^+$	$[C_{27}H_{16}OS_2]^+$	362	1539	CHOS
$[C_{27}H_{23}N_2]^+$	$[C_{32}H_{19}N_2]^+$	3405	4626	CHN
$[C_{26}H_{25}N_2O_2]^+$	$[C_{28}H_{21}N_2O_2]^+$	4805	5447	CHNO
$[C_{24}H_{19}N_2S]^+$	$[C_{28}H_{16}N_2S]^+$	1754	2693	CHNS
$[C_{24}H_{21}N_2OS]^+$	$[C_{27}H_{17}N_2OS]^+$	1418	2230	CHNOS
$[C_{26}H_{16}N_2OS]^+$	$[C_{30}H_{15}N_2O_2]^+$	8791	16846	Zone 1
$[C_{28}H_{36}N_2O_2S]^+$	$[C_{27}H_{33}N_2O_2S_2]^+$	3362	2220	Zone 2
$[C_{26}H_{23}N_2O_2S]^+$	$[C_{29}H_{19}N_2O_2S]^+$	11404	15018	N species
$[C_{29}H_{16}OS]^+$	$[C_{32}H_{16}O_2S_2]^+$	2827	6863	Non-N species
$[C_{14}H_{25}N_2OS]^+$	$[C_{12}H_{21}N_2OS_2]^+$	311	280	Aliphatics
$[C_{17}H_{26}N_2O_2S]^+$	$[C_{14}H_{20}N_2O_2S_2]^+$	982	952	Aromatics
$[C_{28}H_{21}N_2O_2S]^+$	$[C_{31}H_{18}N_2O_2S]^+$	12939	20626	Condensed aromatics
$[C_{27}H_{22}N_2O_2S]^+$	$[C_{30}H_{18}N_2O_2S]^+$	14232	21881	Total

300

301 Among this fraction of Paris IOM, variations in the degree of aromaticity are also observed, especially in
 302 nitrogen-bearing molecules. While non-nitrogen-bearing molecules present a homogeneous aromaticity
 303 ($H/C=0.55$, $O/C=0.03$, $S/C=0.03$), nitrogen-bearing species present two distributions (Figure 2): One displaying
 304 aromaticity near the non-nitrogen-bearing species ($H/C=0.61$, $N/C=0.08$, $O/C=0.04$, $S/C=0.04$), and the other
 305 presenting a much lower aromaticity ($H/C=1.28$, $N/C=0.07$, $O/C=0.07$, $S/C=0.04$). The structure of this low
 306 aromaticity distribution is quite different, presenting molecules with smaller aromatic cores while increasing
 307 aliphatic branching (Figure 4). This observation tends to show that nitrogen could have taken an important role
 308 in the chemical reactivity that led to the formation of these nitrogen-bearing species or that at least two set of
 309 precursors would exist. In addition to these low mass distributions, the presence of condensed aromatic
 310 structures is observed up to the detection of fullerenes that are pure carbon structures. The presence of fullerenes
 311 was already observed with other analytical techniques (Becker et al. 1996, 2000; Berné et al. 2015). These
 312 observations indicate that carbonaceous materials (PAH or hydrogen amorphous carbon (HAC)) are present in
 313 the Paris IOM that could explain the detection of the low mass molecules. Indeed, one plausible interpretation
 314 would be that low mass molecules are probably trapped in large PAH unit by non-covalent hydrophobic
 315 interactions, explaining that they are difficult to extract with classical solvents, and remain associated with the
 316 IOM. This is specially the case for molecules detected at low laser power (11%). The laser enables desorbing
 317 these low mass molecules and then by increasing the laser power (13% to 20%), higher structures can be
 318 desorbed and thus observed. However, at these higher energies (13%, 20 %), a fraction of molecules that were
 319 attached to the PAH/HAC structures by covalent bonds could also be released; their amount is still difficult to
 320 evaluate. In addition, the treatment allowing the isolation of the IOM from the Paris meteorite, and particularly
 321 the acidic hydrolysis, could break some labile acidic chemical functions (Alexander et al. 2017), releasing these
 322 small molecular units that can then be hydrophobically adsorbed on aromatic structures.

323 The complete understanding of mechanisms at the origin of these low mass molecular fractions is currently
324 difficult to apprehend. Different scenarios are generally suggested for explaining the IOM formation: an origin
325 from ISM precursors or during the Solar nebula evolution (Alexander et al. 2017). Concerning the fraction
326 analyzed here, with the high molecular diversity that recalls the one observed for the SOM of the Murchison
327 meteorite (Schmitt-Kopplin et al. 2010), one can suggest that they originate from the processing of dense
328 molecular ices during the protosolar nebula evolution phase (Caselli & Ceccarelli 2012; Tartèse et al. 2018). The
329 chemistry that drives the molecular formation in these environments is mainly related to radical chemistry that
330 occurs at low temperatures followed by an efficient thermal reactivity in the solid phase of the evaporating ices
331 (Fresneau et al. 2017). Indeed, despite such an apparently simple processes, a high diversity of molecules is
332 observed in such astrophysical ice analogs (thousands of molecules with masses up to 4.000 Da (Danger et al.
333 2013)). In addition, it was experimentally shown that when soluble organic molecules from ice analogs are
334 submitted to energetic particles in vacuum (UV photons from the young Sun at the edge of the protoplanetary
335 disk), the formation of an insoluble organic material is observed, a material that could well be then incorporated
336 in small bodies of the solar system (de Marcellus et al. 2017). The composition of both of these organic materials
337 is highly impacted by the presence of nitrogen that drives the chemistry to different molecular families (Fresneau
338 et al. 2017), which could explain the two distributions observed on the nitrogen-bearing species of this Paris
339 IOM. This would imply that before accretion radical chemistry would have driven the reactivity having led to
340 this fraction of IOM, such as observed in ice chemistry experiments. The molecular diversity observed with the
341 LDI analysis of Paris IOM could hence be related to the one generated during the processing of these ice analogs
342 (Danger et al. 2013, 2016). It was indeed observed that the formation of the insoluble material impacts the
343 composition of the soluble fraction suggesting that a continuity may exist between soluble and insoluble
344 materials (Fresneau et al. 2017; Gautier et al. 2020). During their energetic alteration, soluble residues loose
345 labile chemical functions leading to a decrease of their aliphaticity as well as a loss of oxygen and nitrogen
346 (Gautier et al. 2020). This mix of soluble and insoluble organics could then be incorporated inside meteoric
347 parent bodies where they could undergo additional evolution under aqueous alteration conditions (Alexander et
348 al. 2017; Le Guillou & Brearley 2014; Vinogradoff et al. 2020, 2018). First experiments on relevant
349 astrophysical molecules in aqueous alteration conditions have indeed shown that an important reactivity occurs
350 leading to an important molecular reprocessing of the initial organic matter. This process could have also
351 participated to the formation of the both N-bearing groups observed in this work, and drive small hydrophobic
352 molecules to interact with condensed aromatic structures where they could be hydrophobically trapped.

353

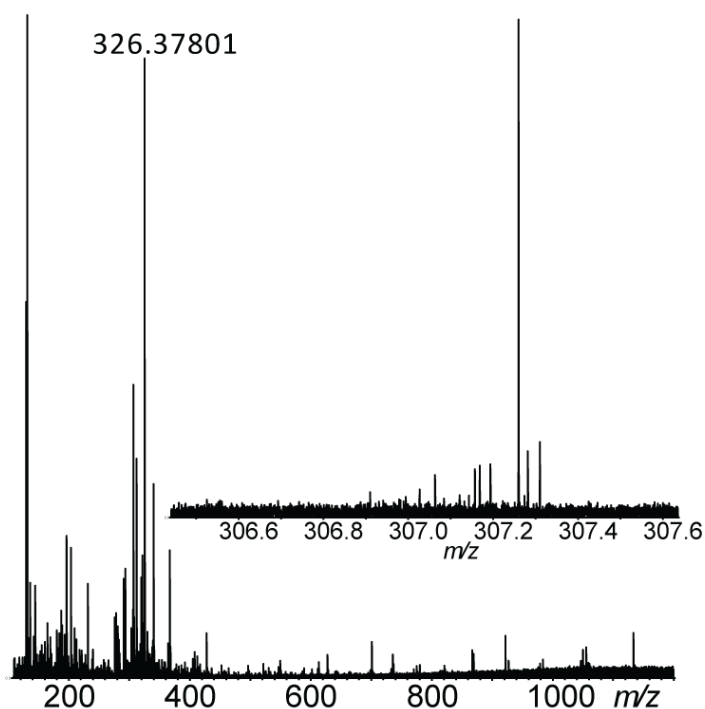
354 5. Conclusions

355 The investigation of IOM in carbonaceous matter is a mature subject that has required many different analytical
356 tools and techniques since more than 30 years. The chemical and isotope signatures of the IOM confirm that it
357 has witnessed the physical and chemical evolution of the transition between the ISM to the solar system. LDI-
358 FT-ICR-MS(/MS) provides here a complementary picture of the composition of the IOM in the Paris meteorite.
359 It exhibits a mix of low mass molecules (100-700 u) presenting high molecular diversity. More than 14000
360 attributions relative to these molecules have been determined, a number increasing with the laser relative power
361 output used for desorbing these molecules. These molecules are trapped within the large aromatic units forming
362 the IOM backbone and have witnessed the same events as the main IOM component. The LDI-FT-ICR-
363 MS(/MS) measurements reported here suggest that a portion of the molecular fragments associated to the IOM
364 structure can be related to chemistry that occurred in ice during the transition from the ISM to the protosolar
365 nebula. This is consistent with the conclusions drawn from H-isotope composition that interstellar like processes
366 have influenced the formation of the IOM precursors. The large molecular diversity evidenced by these
367 measurements of the IOM does echo the large molecular diversity evidenced by FT-ICR investigation of soluble
368 organic compounds in CC; this may question an evolutionary continuity between these soluble and insoluble
369 organic fractions in carbonaceous chondrites.

370

371

373 A.1 Blank sample measured around the position of the Paris IOM (laser energy of 13%).



374

375 **Figure 5** – Blank sample measured around the position of the Paris IOM (laser energy of 13%) with the same
 376 analytical conditions as in section 3.2. No signals related to the Paris IOM are observed.

377

378 A.2 Influence of laser energy

379 The laser power was initially tested to obtain a repeatable LDI FT-ICR mass spectrum with a good S/N. Thus,
 380 laser power of 11 and 13 were tested, as well as 20. The corresponding mass spectra are given in Figure 5 in
 381 which it is shown that an increase of the laser power is responsible for a shift of the mass distribution towards
 382 higher m/z values and an increase of the signals relative to fullerene molecular series increase, especially at 20. It
 383 is well-known that over certain threshold, LDI process is responsible for fragmentation and recombination
 384 reactions (Zhigilei & Garrison 1999). Besides, among the artefacts produced by laser, the presence of fullerenes
 385 in the mass spectra acquired at laser power 13 and 20 has to be interpreted with caution (Santos et al. 2016).

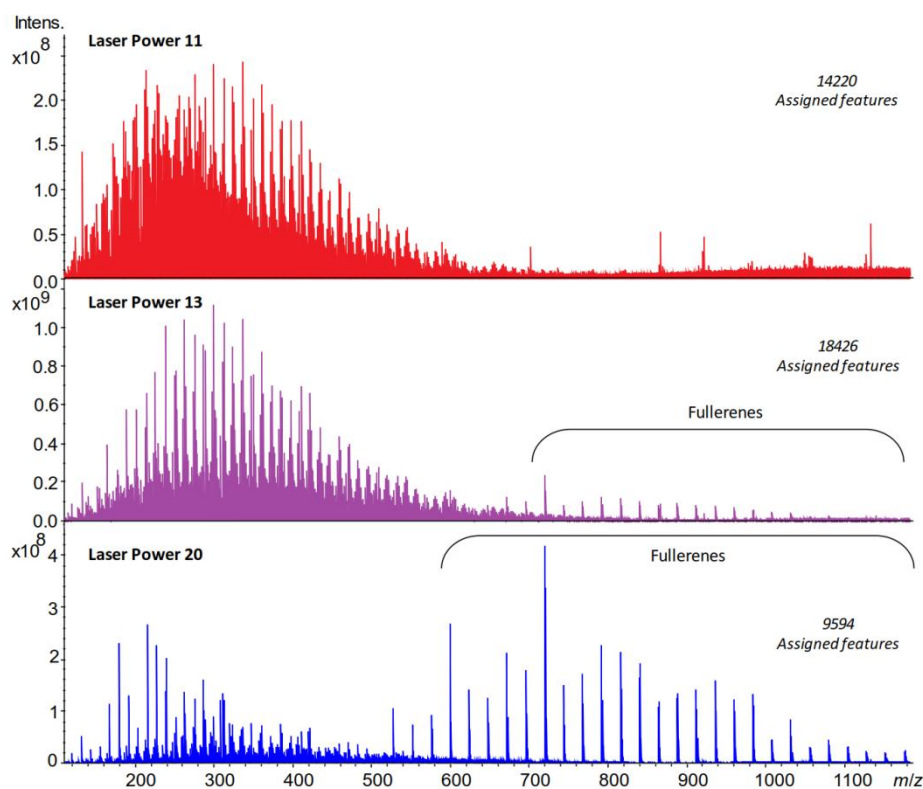
386 The composition description achieved from the different analyses is given in Appendix 2. At laser power 11 and
 387 13, the relative abundances of the different heteroatom classes are close but a higher number of features is
 388 obtained at laser power 13. A deeper insight into the data was done by means of van Krevelen diagrams and H/C
 389 vs. m/z graph (Appendix 2). The van Krevelen diagrams of the data obtained at laser power 20 show that most of
 390 the features are poorly or not oxygenated (low O/C) and highly unsaturated (low H/C). Whereas those achieved
 391 at the two other laser power demonstrate species with higher H/C and O/C values. Thus, most of the species
 392 ionized with the highest laser power are certainly artefacts. The comparison of the graphs H/C vs. m/z obtained
 393 at laser power 11 and 13 evidences that higher-mass compounds for all classes are ionized with higher laser
 394 power. In addition, new unsaturated species ($H/C < 0.2$) are observed whereas at laser power 11, some low-
 395 unsaturated components ($1.75 < H/C < 2$) are exclusively observed. Such a behaviour was also observed by
 396 Aubriet et al. 2018. Therefore, to avoid any misinterpretation of the sample due to laser artefacts, the data
 397 interpretation performed from the mass spectrum acquired with a laser power of 11 will be considered.

398

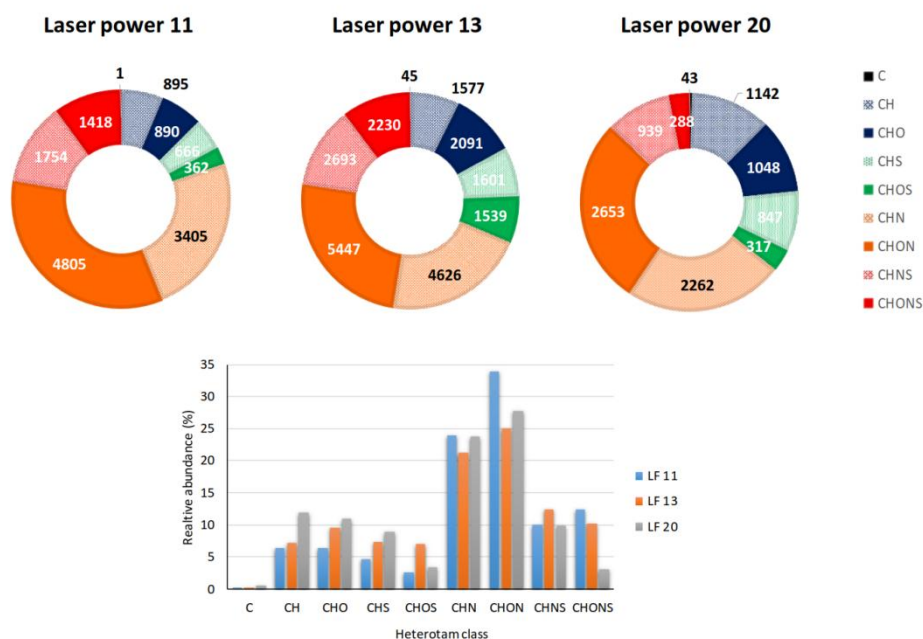
399

400

A

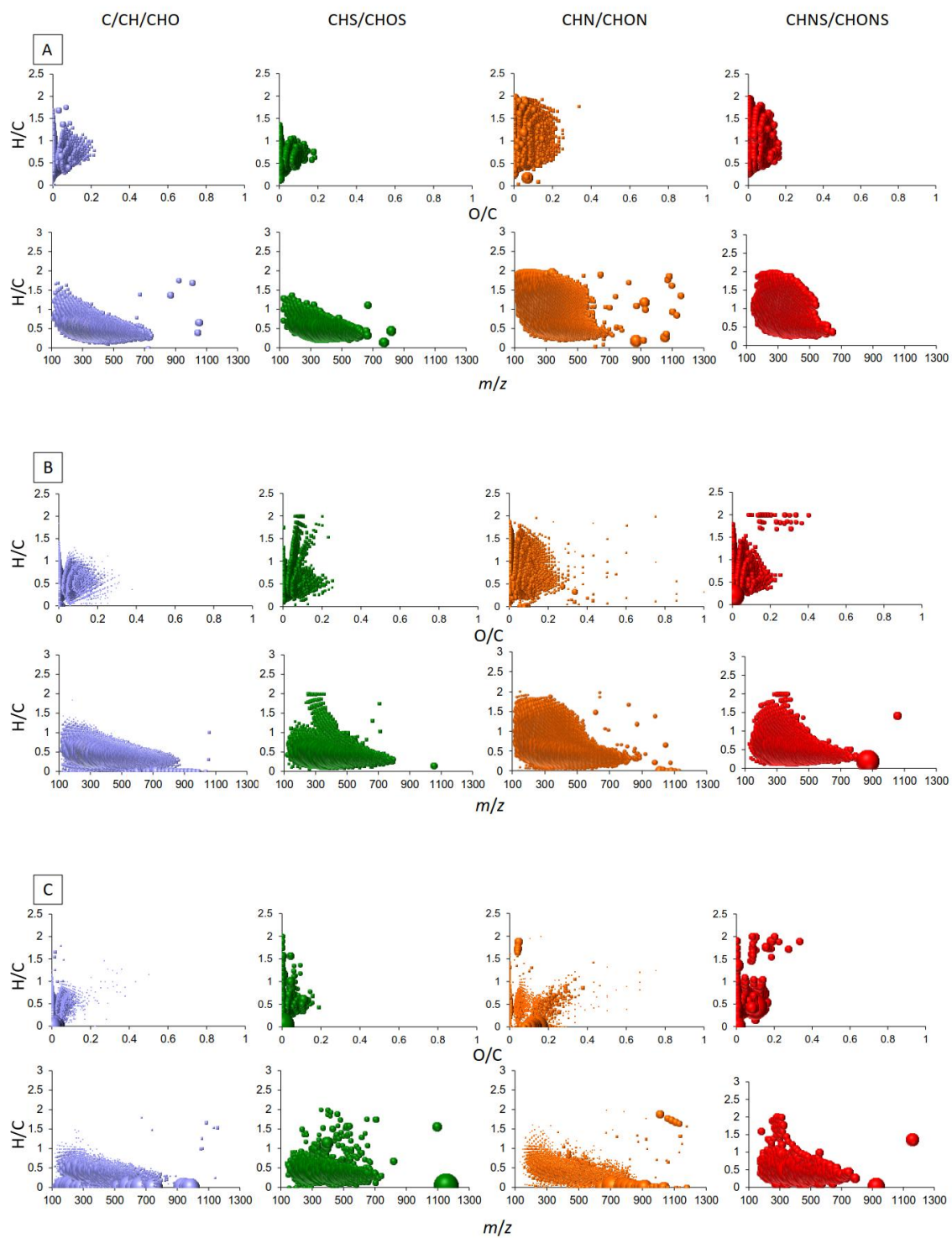


B



401
 402 **Figure 6.** (A) (+) LDI FT-ICR mass spectra of the IOM from Paris meteorite acquired with the laser power of
 403 11, 13, and 20, with the highlight of the clear increase of the signal intensity relative to the fullerene molecular
 404 series. (B) (Top) Pie charts representing the heteroatom class distribution, with the feature numbers, achieved
 405 from (+) LDI FT-ICR MS analysis of the IOM of Paris meteorite with laser power of 11, 13, and 20. (Bottom)
 406 Relative abundances of the different molecular series according to the used laser power.

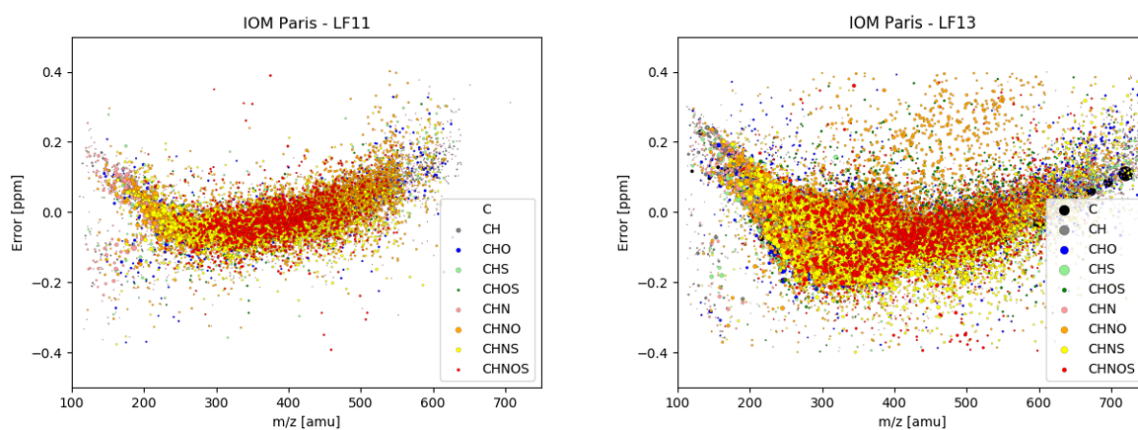
407



408

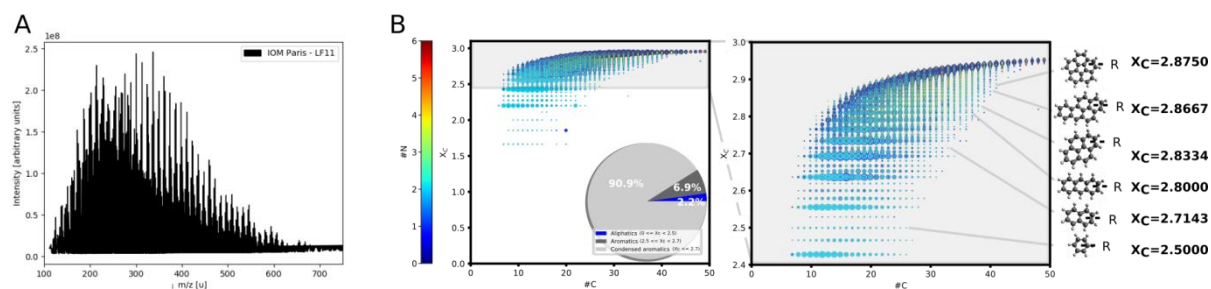
409 **Figure 7.** H/C vs. O/C van Krevelen diagrams and H/C vs. m/z graphs achieved for different heteroatom classes
 410 obtained from (+) LDI FT-ICR MS analysis of the IOM of Paris meteorite at laser power 11 (A), 13 (B), and 20
 411 (% C).
 412

413 **A.3 Error plots related to attributions**



414
415 **Figure 8.** Error plots related to attributions obtained for analyses performed with a laser power of 11% or 13%.
416

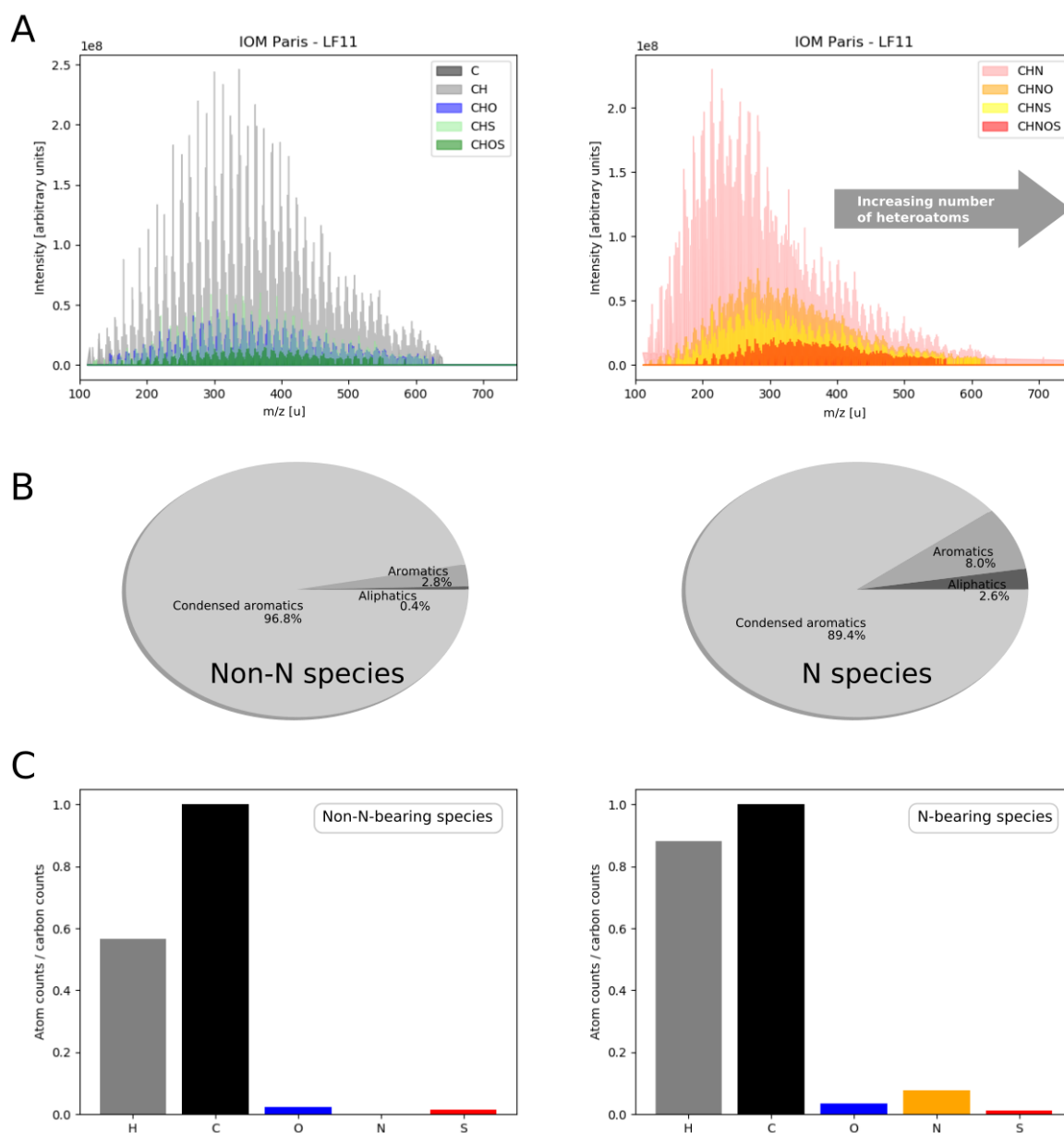
417 **A.4 Xc distribution of molecular formulas**



418
419 **Figure 9** – LDI-FT-ICR mass spectrum (laser power at 11%) of Paris IOM (A) and the Xc distribution of all
420 assigned molecular formulas (B). Xc allows to estimate the degree of unsaturation of carbon atoms on each
421 molecule. It gives an insight on aromaticity of a molecular skeleton.

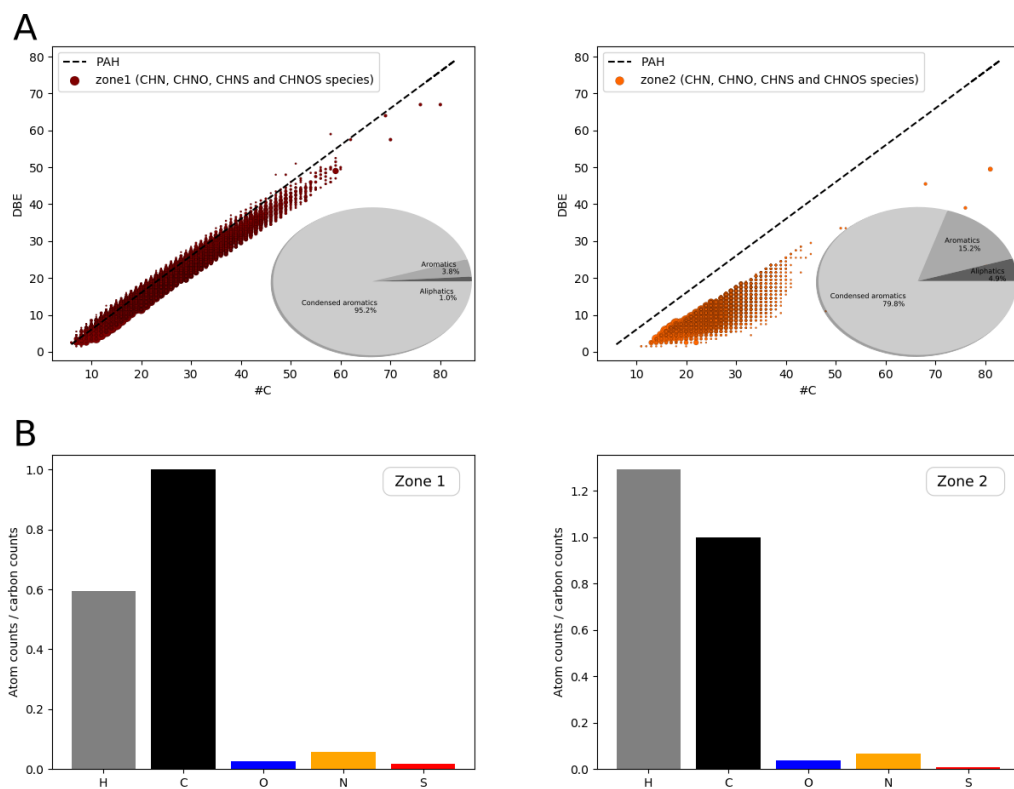
422
423
424
425
426
427
428
429
430
431
432
433

434 **A.5 Characteristic of non-N bearing and N-bearing species**



435

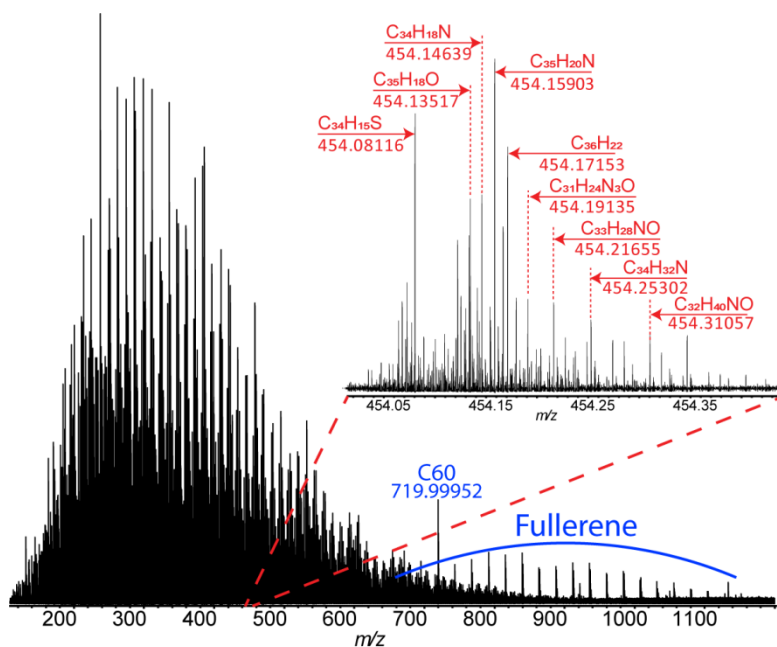
436 **Figure 10** – Mass spectra representing the separated distributions of nitrogen and non-nitrogen species (Figure
 437 1A) where each family is represented by a different color (A). Repartition of the degree of aromaticity
 438 (condensed aromatic, aromatic or aliphatic) based on Xc values (B). The number of atoms relative to the number
 439 of carbon atoms is also presented for nitrogen and non-nitrogen distributions (C).



440

441 **Figure 11** – DBE vs. #C representation for both distributions (zone 1 and zone 2) as defined in Figure 2A (A).
 442 Relative number of atoms to carbon (B).

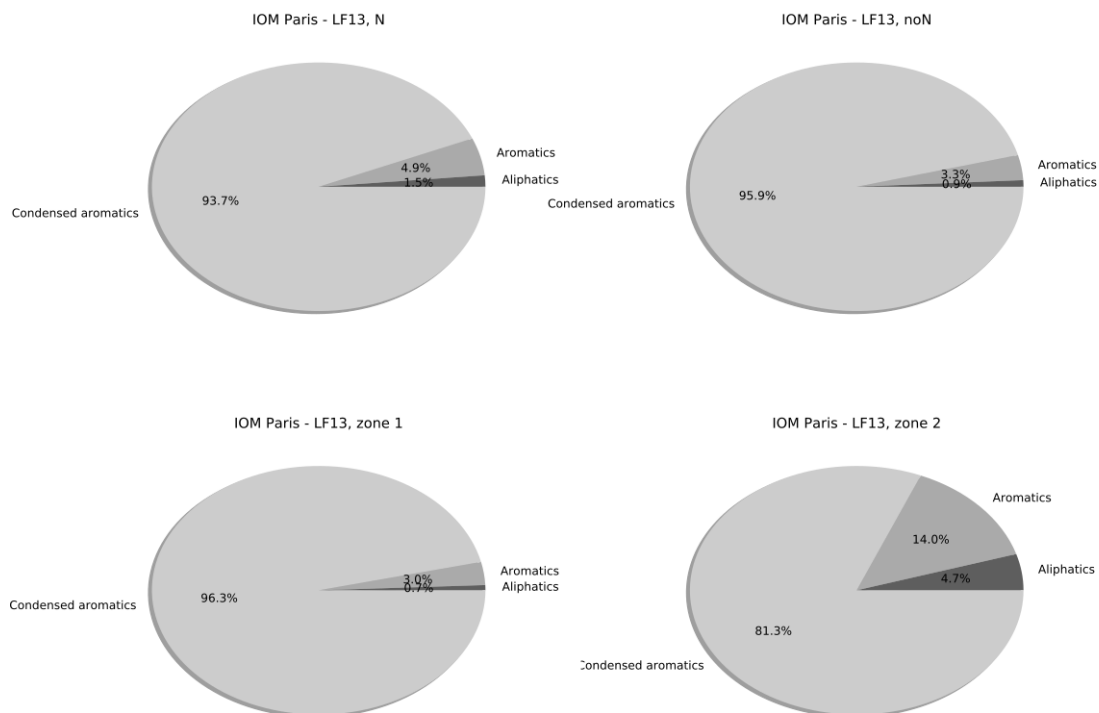
443 **A.6 Detailed Data relative to 13% laser power**



444

445 **Figure 12** – Distributions of nitrogen or non-nitrogen species in the LDI-FT-ICR mass spectrum (laser energy of
 446 13%) of Paris IOM.

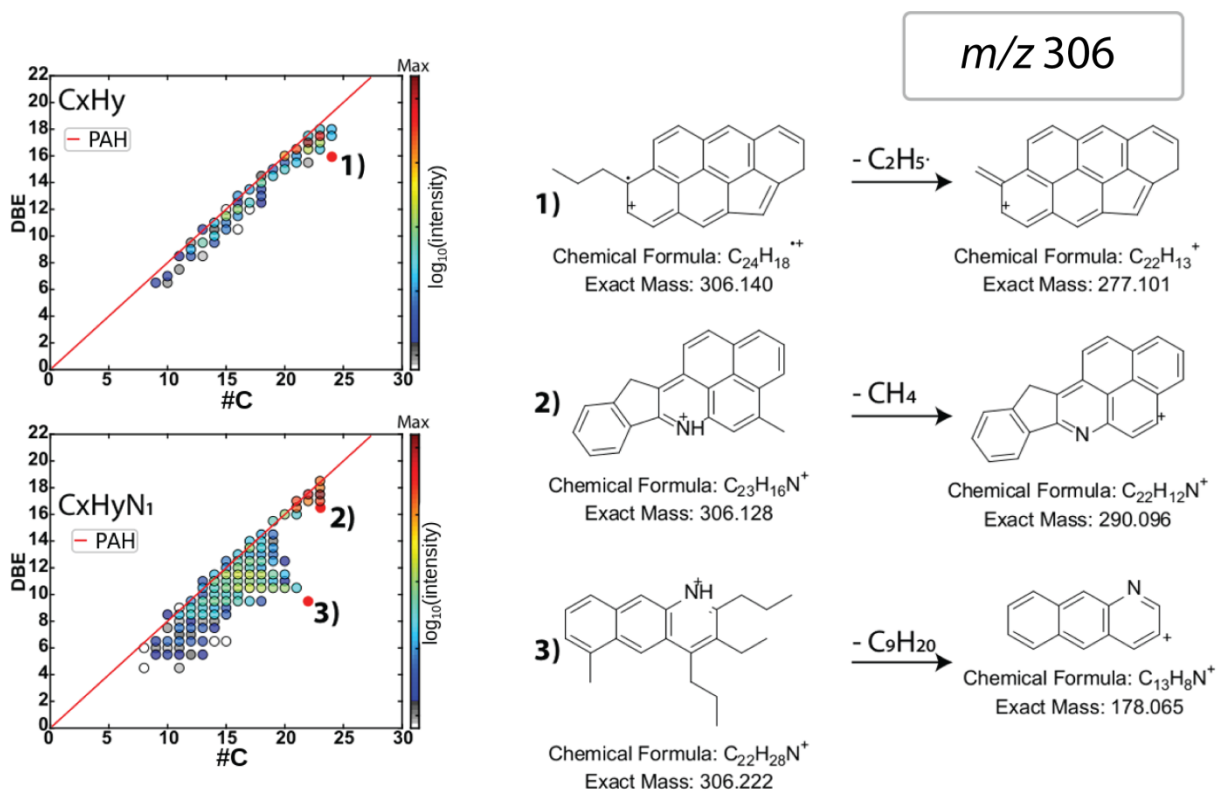
447



448

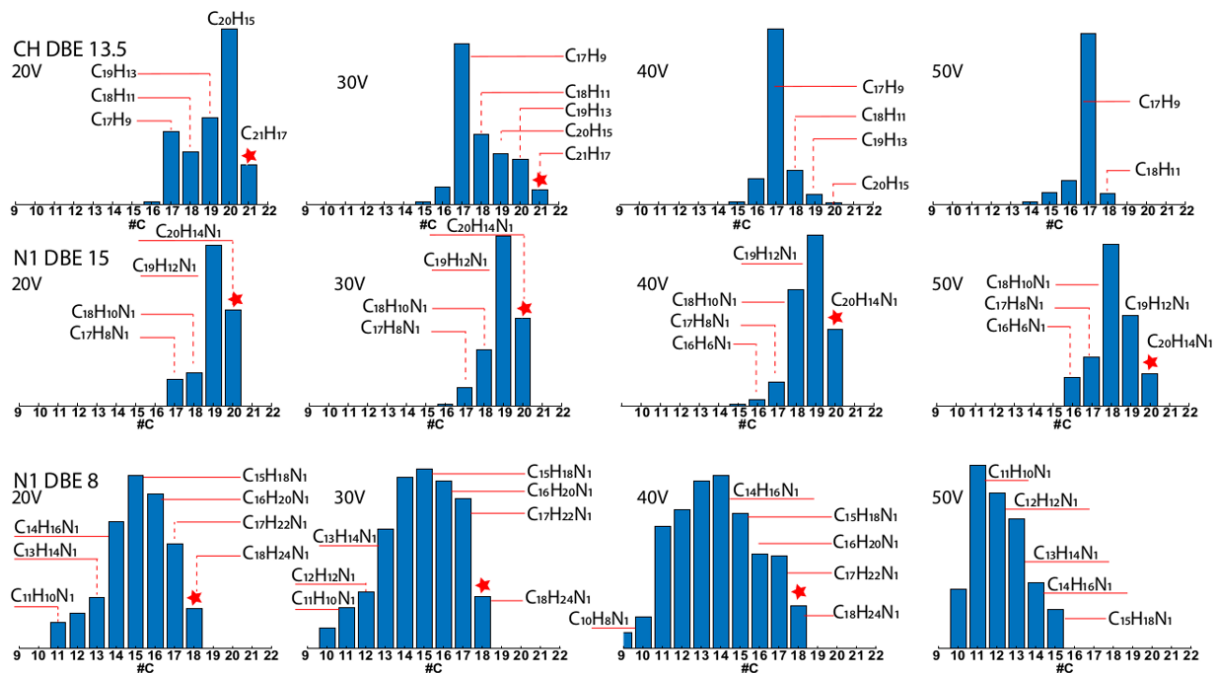
449 **Figure 13** – Repartition of the degree of aromaticity (condensed aromatic, aromatic or aliphatic) based on Xc
 450 values for nitrogen-bearing families, non-nitrogen-bearing families, zone 1 and zone 2.

451 **A.7 Fragmentation patterns of studied ions**



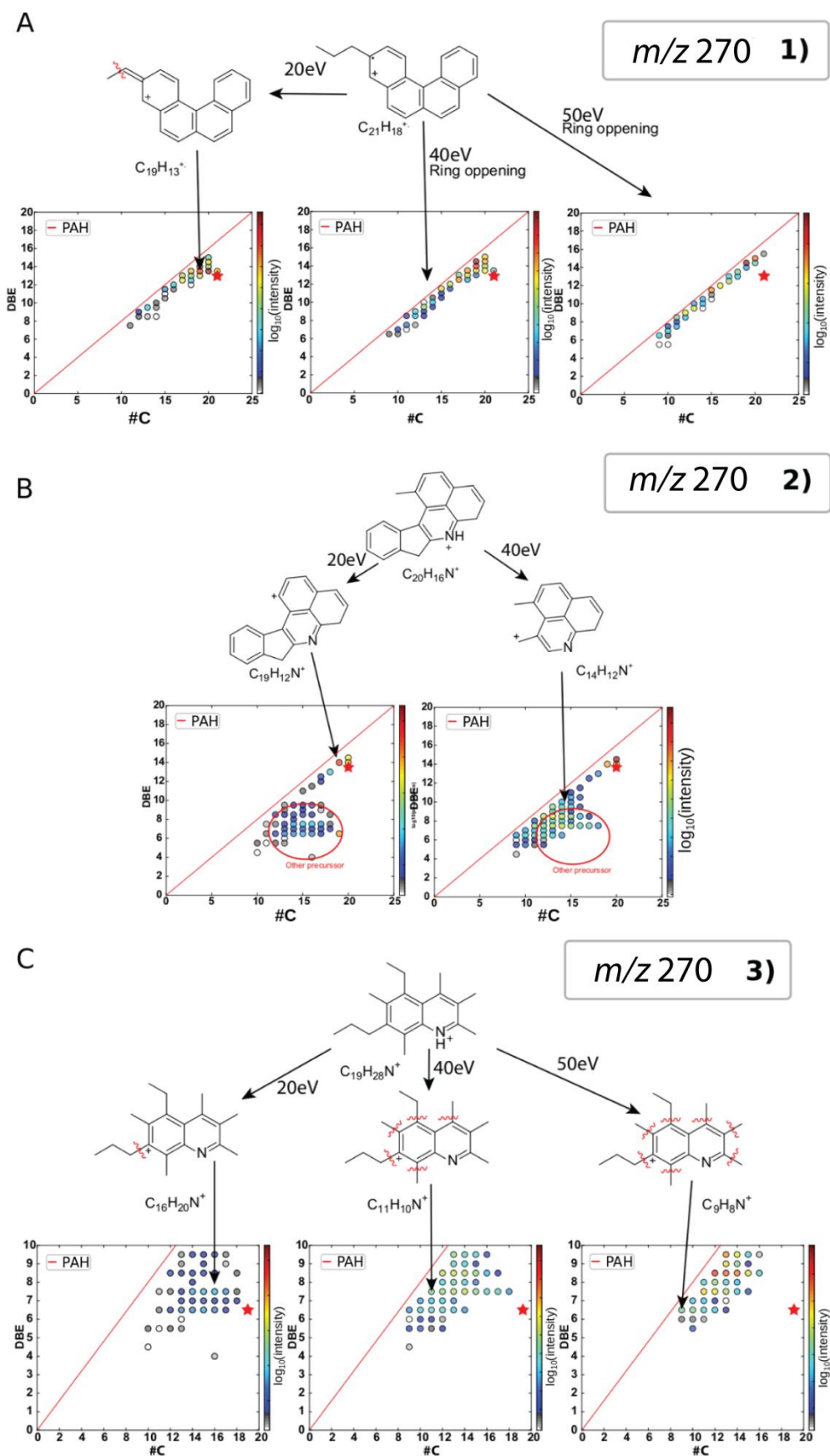
452

453 **Figure 14** - Collision induced dissociation (CID) fragmentation experiments for for IOM Paris, laser energy of
 454 25%. DBE vs #C plots of the CH families CID energies at 40 eV of m/z 306 (A). DBE vs #C maps of the CHN₁
 455 families with CID fragmentation at 40 eV of m/z 306 (B).



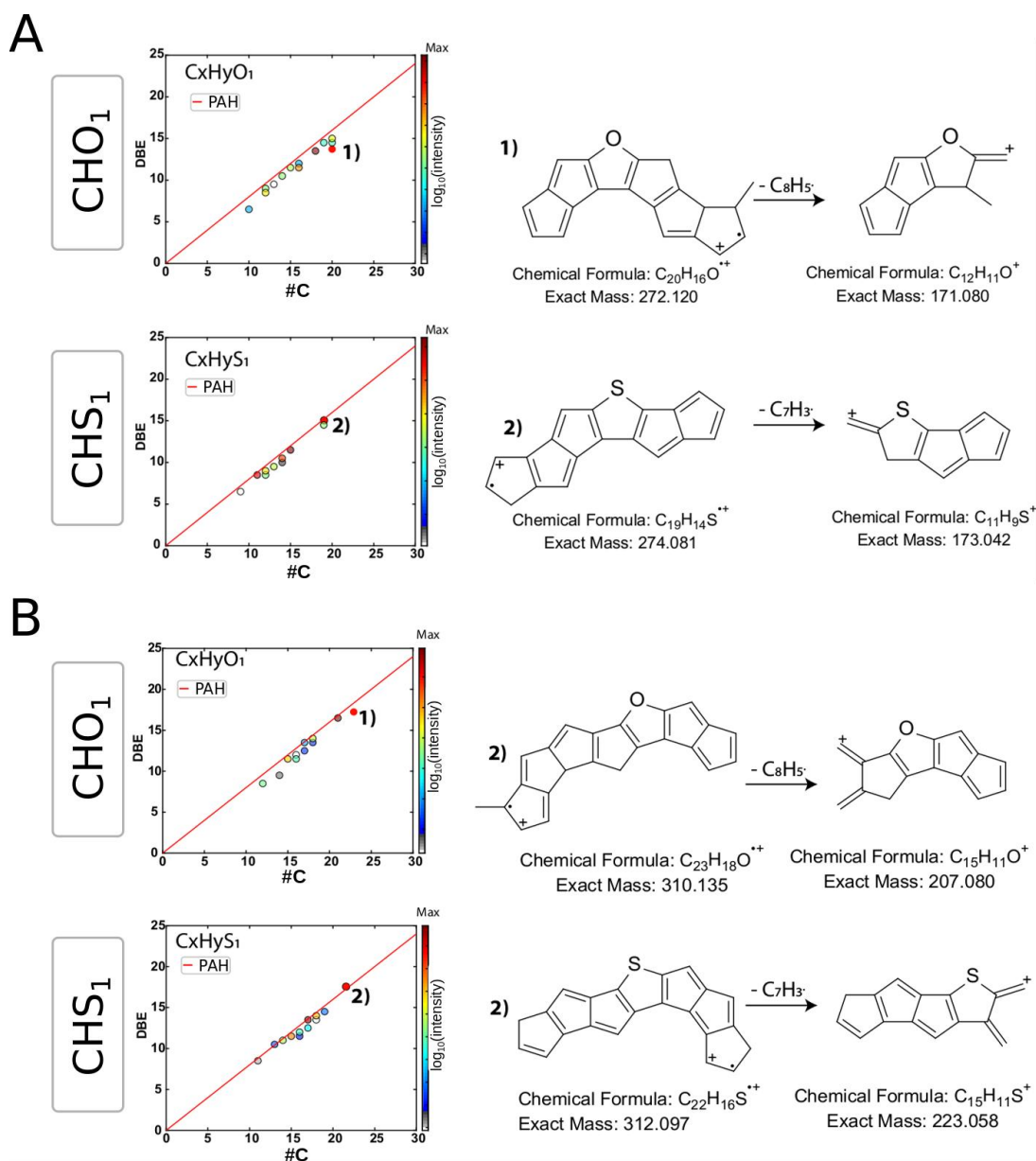
456
 457 **Figure 15** - Bart charts presenting the different fragments (#C) that are generated during the CID at different
 458 energy for molecular ions identified in Figure 6A, B and C. Are also reports de stoichiometric formula for some
 459 fragments.

460
 461
 462
 463
 464
 465
 466
 467
 468
 469
 470
 471
 472
 473



474

475 **Figure 16** - Scheme representing the fragmentation of the ion isolate and shown in Figure 4B 3). The monitoring
 476 of the different fragments allows to determine that the nitrogen is inside the aromatic core and that the parent
 477 structure is branched with aliphatics.



478

479 **Figure 17** - CID fragmentation of CHO₁ and CHS₁ compounds. (A) Example of m/z 272 and 274, respectively.
480 (B) Example of m/z 310 and 312, respectively. Heteroatoms are incorporated in the core of the structures.

481

482 Acknowledgments

483 We are grateful to the meteorite collection of the Muséum National d'Histoire Naturelle in Paris for providing
484 the sample of the Paris meteorite.

485 N.C. and L.R. thank the European Research Council for funding via the ERC projects PrimChem (grant
486 agreement No. 636829.) and HYDROMA (grant agreement No. 819587).

487 This work was supported by the European Regional Development Fund (ERDF) N° HN0001343, the European
488 Union's Horizon 2020 Research Infrastructures program (Grant Agreement 731077), the Région Normandie, and
489 the Laboratoire d'Excellence (LabEx) SynOrg (ANR-11-LABX-0029). Access to a CNRS FTICR research
490 infrastructure (FR3624) is gratefully acknowledged.

491 G.D., A.R. and L.R. thank the Agence nationale de la recherche (RAHIIA_SSOM, ANR-16-CE29-0015), the
492 Centre National d'Etudes Spatiales from its exobiology program, and the Centre National de la Recherche
493 Française (CNRS, "Physique et Chimie du Milieu Interstellaire" (PCMI) and "Programme National de
494 Planétologie" (PNP) programs) for their financial support.

495 **References**

496 Alexander, C. M. O., Cody, G. D., De Gregorio, B. T., Nittler, L. R., & Stroud, R. M., *Chemie der Erde -*
497 *Geochemistry*, 77 (Elsevier GmbH.), 227, (2017)

498 Alexander, C. M. O., Fogel, M. L., Yabuta, H., & Cody, G. D., *Geochem Cosmo Acta*, 71, 4380, (2007)

499 Aubriet, F., Ghislain, T., Hertzog, J., et al., *J Am Soc Mass Spectrom*, 29, 1951, (2018)

500 Barrère, C., Hubert-Roux, M., Lange, C. M., et al., *Rapid Commun Mass Spectrom*, 26, 1347, (2012)

501 Becker, L., Poreda, R. J., & Bada, J. L., *Science* (80-), 272, 249, (1996)

502 Becker, L., Poreda, R. J., & Bunch, T. E., *Proc Natl Acad Sci U S A*, 97, 2979, (2000)

503 Berné, O., Montillaud, J., & Joblin, C., *Astron Astrophys*, 577, A133, (2015)

504 Caselli, P., & Ceccarelli, C., *Astron Astrophys Rev*, 20, 56, (2012)

505 Chacón-Patiño, M. L., Rowland, S. M., & Rodgers, R. P., *Energy & Fuels*, 31, 13509, (2017)

506 Chacón-Patiño, M. L., Rowland, S. M., & Rodgers, R. P., *Energy & Fuels*, 32, 9106, (2018), (a)

507 Chacón-Patiño, M. L., Rowland, S. M., & Rodgers, R. P., *Energy & Fuels*, 32, 314, (2018), (b)

508 Cho, Y., Jin, J. M., Witt, M., et al., *Energy & Fuels*, 27, 1830, (2013)

509 Cody, G. D., & Alexander, C. M. O., *Geochim Cosmochim Acta*, 69, 1085, (2005)

510 Cody, G. D., Alexander, C. M. O., & Tera, F., *Geochim Cosmochim Acta*, 66, 1851, (2002)

511 Cody, G. D., Heying, E., Alexander, C. M. O., et al., *Proc Natl Acad Sci*, 108, 19171, (2011)

512 Danger, G., Fresneau, A., Abou Mrad, N., et al., *Geochim Cosmochim Acta*, 189, 184, (2016)

513 Danger, G., Orthous-Daunay, F., de Marcellus, P., et al., *Geochim Cosmochim Acta*, 118, 184, (2013)

514 Derenne, S., & Robert, F., *Meteorit Planet Sci*, 45, 1461, (2010)

515 Fresneau, A., Mrad, N. A., LS d'Hendecourt, L., et al., *Astrophys J*, 837 (IOP Publishing), 168, (2017)

516 Gardinier, A., Derenne, S., Robert, F., et al., *Earth Planet Sci Lett*, 184, 9, (2000)

517 Gautier, T., Danger, G., Mousis, O., et al., *Earth Planet Sci Lett*, 531 (Elsevier B.V.), 116011, (2020)

518 Göpel, C., Birck, J.-L., Galy, A., Barrat, J.-A., & Zanda, B., *Geochim Cosmochim Acta*, 156, 1, (2015)

519 Le Guillou, C., & Brearley, A., *Geochim Cosmochim Acta*, 131, 344, (2014)

520 Hayatsu, R., Matsuoka, S., Scott, R. G., Studier, M. H., & Anders, E., *Geochim Cosmochim Acta*, 41, 1325,
521 (1977)

522 Hertkorn, N., Harir, M., & Schmitt-Kopplin, P., *Magn Reson Chem*, 53, 754, (2015)

523 Hewins, R. H., Bourot-Denise, M., Zanda, B., et al., *Geochim Cosmochim Acta*, 124, 190, (2014)

524 Kanawati, B., Bader, T. M., Wanczek, K.-P., Li, Y., & Schmitt- Kopplin, P., *Rapid Commun Mass Spectrom*,
525 31, 1607, (2017)

- 526 Leroux, H., Cuvillier, P., Zanda, B., & Hewins, R. H., *Geochim Cosmochim Acta*, 170, 247, (2015)
- 527 Maillard, J., Carrasco, N., Schmitz-Afonso, I., Gautier, T., & Afonso, C., *Earth Planet Sci Lett*, 495 (Elsevier
528 B.V.), 185, (2018)
- 529 Le Maître, J., Hubert-Roux, M., Paupy, B., et al., *Faraday Discuss*, 218, 417, (2019)
- 530 de Marcellus, P., Fresneau, A., Brunetto, R., et al., *Mon Not R Astron Soc*, 464, 114, (2017)
- 531 Marrocchi, Y., Gounelle, M., Blanchard, I., Caste, F., & Kearsley, A. T., *Meteorit Planet Sci*, 49, 1232, (2014)
- 532 Modica, P., Martins, Z., Meinert, C., Zanda, B., & d'Hendecourt, L. L. S., *Astrophys J*, 865 (IOP Publishing),
533 41, (2018)
- 534 Orthous-Daunay, F.-R.-R., Quirico, E., Beck, P., et al., *Icarus*, 223, 534, (2013)
- 535 Orthous-Daunay, F.-R., Quirico, E., Lemelle, L., et al., *Earth Planet Sci Lett*, 300, 321, (2010)
- 536 Pearson, V. K., Sephton, M. A., Franchi, I. A., Gibson, J. M., & Gilmour, I., *Meteorit Planet Sci*, 41, 1899,
537 (2006)
- 538 Pereira, T. M. C., Vanini, G., Tose, L. V., et al., *Fuel*, 131 (Elsevier Ltd), 49, (2014)
- 539 Pizzarello, S.; Cooper, G. W.; Flynn, G. J., in *Meteorites and the Early Solar System II*, p. 625, (2006)
- 540 Qi, Y., Witt, M., Jertz, R., et al., *Rapid Commun Mass Spectrom*, 26, 2021, (2012)
- 541 Remusat, L., in *EMU Notes in Mineralogy - volume 15: Planetary Mineralogy*, ed. M. R. Lee, & H. Leroux (The
542 European Mineralogical Union), 33, (2015)
- 543 Remusat, L., Derenne, S., & Robert, F., *Geochim Cosmochim Acta*, 69, 4377, (2005), (a)
- 544 Remusat, L., Derenne, S., Robert, F., & Knicker, H., *Geochim Cosmochim Acta*, 69, 3919, (2005), (b)
- 545 Remusat, L., Guan, Y., Wang, Y., & Eiler, J. M., *Astrophys J*, 713, 1048, (2010)
- 546 REMUSAT, L., GUILLOU, C., ROUZAUD, J.-N., et al., *Meteorit Planet Sci*, 43, 1099, (2008)
- 547 Rubin, A. E., Trigo-Rodríguez, J. M., Huber, H., & Wasson, J. T., *Geochem Cosmo Acta*, 71, 2361, (2007)
- 548 Ruf, A., D'Hendecourt, L., & Schmitt-Kopplin, P., *Life*, 8, 18, (2018)
- 549 Ruf, A., Poinot, P., Geffroy, C., D'Hendecourt, L. L. S., & Danger, G., *Life*, 9, 1, (2019)
- 550 Santos, V. G., Fasciotti, M., Pudenzi, M. A., et al., *Analyst*, 141 (Royal Society of Chemistry), 2767, (2016)
- 551 Schmitt-Kopplin, P., Gabelica, Z., Gougeon, R. D., et al., *Proc Natl Acad Sci U S A*, 107, 2763, (2010)
- 552 Schmitt-Kopplin, P., Herir, M., Kanawati, B., et al., *Meteorites*, 2, 79, (2012)
- 553 Sephton, M. A., *Nat Prod Rep*, 19 (The Royal Society of Chemistry), 292, (2002)
- 554 Tartèse, R., Chaussidon, M., Gurenko, A., Delarue, F., & Robert, F., *Proc Natl Acad Sci*, 115, 8535, (2018)
- 555 Vinogradoff, V., Bernard, S., Le Guillou, C., & Remusat, L., *Icarus*, 305, 358, (2018)
- 556 Vinogradoff, V., Le Guillou, C., Bernard, S., et al., *Geochim Cosmochim Acta*, 212 (Elsevier Ltd), 234, (2017)
- 557 Vinogradoff, V., Le Guillou, C., Bernard, S., et al., *Geochim Cosmochim Acta*, 269 (Elsevier Ltd), 150, (2020)
- 558 Wang, N., Zhi, Y., Wei, Y., et al., *Nat Commun*, 11, 1079, (2020)
- 559 Wu, Q., Pomerantz, A. E., Mullins, O. C., & Zare, R. N., *J Am Soc Mass Spectrom*, 24, 1116, (2013)

- 560 Yabuta, H., Naraoka, H., Sakanishi, K., & Kawashima, H., *Meteorit Planet Sci*, 40, 779, (2005)
- 561 Yassine, M. M., Harir, M., Dabek-Zlotorzynska, E., & Schmitt-Kopplin, P., *Rapid Commun Mass Spectrom*, 28,
562 2445, (2014)
- 563 Zhigilei, L. V., & Garrison, B. J., *Appl Phys Lett*, 74, 1341, (1999)
- 564